

Effect of wind veer on wind turbine power generation

Cite as: Phys. Fluids **33**, 015101 (2021); <https://doi.org/10.1063/5.0033826>

Submitted: 19 October 2020 . Accepted: 10 December 2020 . Published Online: 04 January 2021

 Linyue Gao (高琳越), Bochen Li (李伯宸), and  Jiarong Hong (洪家荣)



[View Online](#)

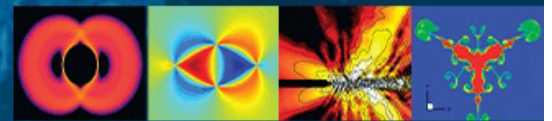


[Export Citation](#)



[CrossMark](#)

Physics of Fluids
GALLERY OF COVERS



Effect of wind veer on wind turbine power generation

Cite as: *Phys. Fluids* **33**, 015101 (2021); doi: [10.1063/5.0033826](https://doi.org/10.1063/5.0033826)

Submitted: 19 October 2020 • Accepted: 10 December 2020 •

Published Online: 4 January 2021



View Online



Export Citation



CrossMark

Linyue Gao (高琳越),¹  Bochen Li (李伯宸),² and Jiarong Hong (洪家荣)^{1,2,a)} 

AFFILIATIONS

¹St. Anthony Falls Laboratory, University of Minnesota, Minneapolis, Minnesota 55414, USA

²Department of Mechanical Engineering, University of Minnesota, Minneapolis, Minnesota 55455, USA

^{a)} Author to whom correspondence should be addressed: jhong@umn.edu

ABSTRACT

Wind direction variation with height (wind veer) plays an essential role in the inflow wind field as the wind turbine enlarges. We explore the wind veer characteristics and their impact on turbine performance using a 5-year field dataset measured at the Eolos Wind Energy Research Station of the University of Minnesota. Wind veer exhibits an appreciable diurnal variation that veering and backing winds tend to occur during nighttime and daytime, respectively. We further propose to divide the wind veer conditions into four scenarios based on their changes in turbine upper and lower rotors that influence the loading on different rotor sections: VV (upper rotor: veering, lower rotor: veering), VB (upper rotor: veering, lower rotor: backing), BV (upper rotor: backing, lower rotor: veering), and BB (upper rotor: backing, lower rotor: backing). Such a division allows us to elucidate better the impact of wind veer on turbine power generation. The clockwise-rotating turbines tend to yield substantial power losses in scenarios VV and VB and small power gains in scenarios BV and BB. The counterclockwise-rotating turbines follow exactly opposite trends to the clockwise turbine. The derived findings are generalizable to other wind sites for power evaluation and provide insights into the turbine type selections targeting the maximum profits.

Published under license by AIP Publishing. <https://doi.org/10.1063/5.0033826>

I. INTRODUCTION

The terminology of “wind veer” refers to the wind direction variation with height in the community of meteorology, primarily due to the Ekman spiral related to the balance on Coriolis force, pressure gradient force and friction, advection turning associated with thermal wind, and inertial oscillation.¹ Wind veer can be categorized as veering wind and backing wind regarding the wind spiral direction. In the Northern Hemisphere, the veering wind turns clockwise (CW), and it is usually associated with warm air advection and dynamic lifting, primarily because a south wind transports more heated air to the north. The backing wind turns counterclockwise (CCW) with height and is usually related to cold air advection and dynamic sinking.¹ In recent years, the wind veer effect is becoming an increasingly significant issue in the community of wind energy as the wind turbines continue to grow in size. Up to now, the largest offshore wind turbine (Haliade-X 12 MW) reaches 370 m with a hub height of $H = 260$ m and a rotor diameter of $D = 220$ m. The prototype of a more powerful offshore turbine (SG 14-222 DD, 14 MW,

$D = 222$ m) unveiled by Siemens Gamesa is to be ready by 2021. Even the onshore wind turbine (Siemens 5.8 MW) can also reach up to 250 m with a site-specific hub height up to $H = 165$ m and a rotor diameter of $D = 170$ m. Such heights are far beyond the surface layer below ~ 100 m associated with strong vertical wind shear and fall into the range of Ekman layers with substantial changes in wind directions due to the Ekman spiral effect as a consequence of the Coriolis force. Therefore, a better understanding of how wind turbines/wind farms behave under wind veer conditions is highly needed for turbine maximization.

As a phenomenon of the atmospheric boundary layer flows, the wind veer effect is not fully considered in most previous simulation investigations²⁻⁴ and wind tunnel studies^{5,6} on the wind farm flows. There are only a few state-of-the-art literature studies that extensively discuss the turbine related wind veer effect, which can be summarized into three aspects: wind veer characteristics⁷⁻⁹ and their impacts on turbine power production¹⁰⁻¹² and turbine wake deflection.¹³⁻¹⁶ Wind veer may present appreciable differences between diurnal and nocturnal periods or seasons. Walter *et al.*⁷

characterized the wind veer over a span from 10 m to 116 m using a 7523-h (313-day) dataset measured by a meteorological tower (met tower) located in Texas, USA. They found that the wind veer follows a daily cycle that the stable nighttime conditions permit a higher probability of high-magnitude veering wind. Similar trends were also extracted for turbines (Vestas V80-2MW, $H = 70$ m and $D = 80$ m) under onshore atmospheric boundary layer conditions by Abkar *et al.*⁸ using large-eddy simulations (LESs) combined with the actuator-disk model for turbines. They reported that wind veer is more substantial ($0.10^\circ/\text{m}$ – $0.25^\circ/\text{m}$) at the nocturnal time associated with a stable atmosphere, while weaker wind veer tends to occur at daytime ($<0.02^\circ/\text{m}$) with convective flows. Regarding the offshore site, Bodini *et al.*⁹ investigated the atmospheric boundary layer over the span of a turbine rotor (Siemens Gamesa 7.0 MW, $D = 154$ m) based on a 13-month lidar measurement deployed on a platform off the Massachusetts coast, USA. They reported that wind veer is much stronger in summer ($0.10^\circ/\text{m}$, winter: $0.05^\circ/\text{m}$) when the wind flows from land, similar to the stable nighttime conditions found onshore.⁷ Such annual variations of wind veer in onshore sites are still unclear, which may significantly differ from the offshore observations due to the different atmospheric conditions, such as higher turbulence dissipation.⁹

With a better understanding of the wind veer characteristics, several field studies are conducted to investigate the wind veer effect on wind turbine power performance.^{10–12} Bardal *et al.*¹⁰ conducted a ten-month lidar measurement for 3 MW turbines on the coast of Mid-Norway and pointed out that the wind veer may have a small effect on the overall turbine power performance. However, high veer conditions may be associated with appreciable power reduction. They also found that the power coefficient (C_p) decreases with inflow wind speeds ranging from ~ 6 m/s to 11 m/s (below the rated speed). However, an opposite trend that C_p increases below the rated wind speed and decreases above the rated speed was reported by Sakagami and Taves *et al.*¹¹ based on a six-month field measurement for 0.9 MW turbines ($D = 44$ m and $H = 55$ m) located on the northeast coast of Brazil. Such conflicting statements are suggested to be associated with different locations, data acquisition time, and diverse analysis methods. In addition to the studies using the absolute value of wind veer, the investigation conducted by Gomez and Lundquist¹² reported the different effects of veering and backing winds on turbine power (1.5 MW, $D = 82.5$ m and $H = 80$ m) using a three-month lidar dataset measured at Iowa, USA. They found that the large veering has more significant detrimental effects on the turbine power compared to the small backing winds. They also highlighted that the larger wind veer that occurs during a period of ramping electricity demand (06:00–09:00 local time in the morning) undermines turbine power by more than 10%. The aforementioned findings are valuable to provide insight into the optimization of turbine operations for better power generation. However, those field tests usually last for less than one year due to the lack of well-equipped test facilities or the challenges in the long-term measurements. It is critical to conduct long-term field measurements to reduce the uncertainties induced by the seasonal differences or influence of annual variability to draw conclusions.

Such field measurements can also provide realistic inflow conditions that can be used for the numerical simulations to investigate the wind veer effect on turbine wake deflection. So far, there is no

simulation using realistic inflow conditions. Both simulation works for individual turbines and turbine arrays (or wind farms) are conducted under much-simplified wind veer conditions.^{13–16} Van der Laan and Sørensen¹³ simulated an NREL 5 MW turbine ($D = 126$ m and $H = 90$ m) under wind veer conditions and reached a consensus about the wake deflection direction (clockwise in the Northern Hemisphere). Their work proved that the Coriolis force indirectly causes the turbine wake to deflect clockwise because of the presence of wind veer and not because of the local changes in the Coriolis force. Englberger *et al.*¹⁵ simulated a turbine ($D = 100$ m and $H = 100$ m) under wind veer and no veer conditions and found that the rotor rotational direction impacts the wake deflection in the presence of wind veer. If no veer is present, the rotor rotation direction exerts little impact. As for wind turbine arrays, Howland *et al.*¹⁴ used a Coriolis force term to introduce the wind veer effect in their simulation and found that veer redistributes Reynolds stresses that may have notable impact on wake recovery. Gadde and Stevens¹⁶ simulated a 30-turbine site ($D = 100$ m and $H = 100$ m) and pointed out that a strong wind veer tends to lead to more pronounced wake deflection and such deflection has a significant impact on the power of wind turbines further downstream.

In summary, the existing field studies lack consistent conclusions in terms of how wind veer affects the turbine power generation. Additionally, the improvement in current simulations significantly relies on the field data to provide realistic wind veer inflow characteristics. Consequently, in the present study, we seek to provide a systematic evaluation of wind veer characteristics, including both daily and annual variations, and their effects on turbine power performance, by leveraging the long-term field database measured at the Eolos Wind Energy Research Station of the University of Minnesota (referred to as the Eolos station hereafter). Section II describes the experimental facilities at the Eolos station and the data preprocessing methods. Section III introduces a novel concept of four scenarios for wind veer concerning its interaction with the turbine rotor, followed by a detailed wind veer characterization and its impact on turbine power generation. Section IV concludes with the main findings of the present study and briefly discusses how to improve wind turbine power performance under wind veer conditions.

II. METHODOLOGY

A. Experimental facilities

Our investigation utilizes the field data collected at the Eolos Station of the University of Minnesota in Rosemount, Minnesota ($44^\circ 44' 01.4''\text{N}$, $93^\circ 05' 04.4''\text{W}$). The station is located in a nearly flat terrain with a few sparse roughness elements such as scattered 12-story buildings and tree patches, whose influence zone is limited to ~ 6 m above the ground based on our past atmospheric boundary layer measurements.¹⁷ The station consists of a 2.5 MW upwind, three-bladed, horizontal-axis wind turbine (Clipper Liberty C96, referred to as the Eolos turbine hereafter) and a 130 m meteorological tower (referred to as the met tower hereafter),^{18–20} as shown in Fig. 1(a). The met tower is located 170 m ($1.77 D$) south [i.e., along one of the prevailing wind directions, 180° , see Fig. 1(b)] to the turbine. The met tower is well-instrumented with velocity (sonic, and cup and vane anemometers), temperature, and relative humidity sensors to characterize the inflow conditions for the turbine. Four

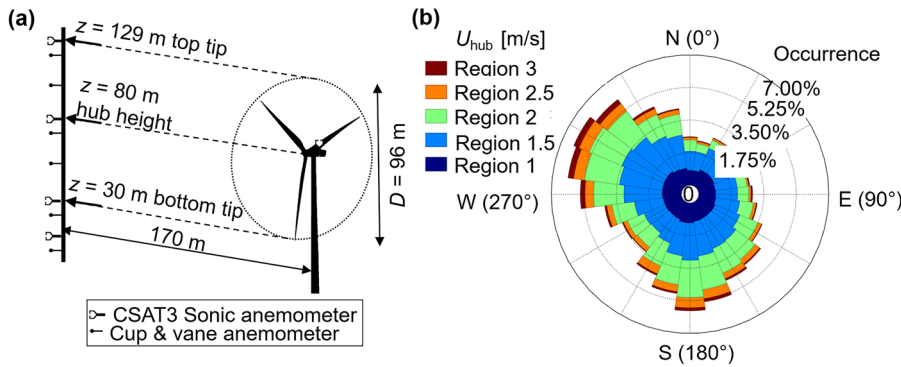


FIG. 1. (a) Schematic of the 2.5 MW wind turbine and the meteorological tower at the station. (b) Wind rose based on the measured wind direction and wind speed at hub height in the recent five years. The percent level indicates the occurrence of a specific case in a 15° wind direction sector. “N,” “E,” “S,” and “W” stand for the north, east, south, and west directions, respectively.

high-resolution sonic anemometers (Campbell Scientific, CSAT3) are mounted at four representative elevations, i.e., rotor top tip ($z = 129$ m), hub height ($z = 80$ m), rotor bottom tip ($z = 30$ m), and standard 10 m. Six cup and vane anemometers (Met One, 014-A) with a sampling rate of 1 Hz are installed 3 m below each sonic anemometer, i.e., at 126 m, 77 m, 27 m, and 7 m, and at two other elevations, i.e., 102 m and 52 m, corresponding to the midspans of lower and upper blades, respectively. The wind direction measurement accuracy of the sonic anemometers (Campbell Scientific, CSAT3) used in the present study is $\pm 0.7^\circ$ at 1 m/s.

The turbine belongs to International Electric Commission (IEC) turbine class II with a rotor diameter of $D = 96$ m and a hub height of $H = 80$ m. The cut-in, rated, and cut-out wind speeds are ~ 4.0 m/s, 11.0 m/s, and 25.0 m/s, respectively. The turbine operates with various regulation strategies under five regions. Specifically, the turbine is in control of region 1 ($U_{hub} < 4.0$ m/s) with no power generation when the wind speed at hub height (U_{hub}) is lower than the cut-in wind speed. The turbine operates in region 3 ($U_{hub} > 11.0$ m/s) with variable-pitch regulation when U_{hub} is higher than the rated wind speed. The turbine is variable-speed regulated when U_{hub} is between the cut-in and rated wind speeds, including region 1.5 ($4.0 \text{ m/s} \leq U_{hub} < 6.9 \text{ m/s}$), region 2 ($6.9 \text{ m/s} \leq U_{hub} < 9.2 \text{ m/s}$), and region 2.5 ($9.2 \text{ m/s} \leq U_{hub} < 11.0 \text{ m/s}$). Note that the turbine possesses the optimal performance with the maximum power coefficient ($C_{p,max} = 0.472$) in region 2, and region 1.5 and region 2.5 are transitional regions. As shown in the wind rose in Fig. 1(b), the probabilities of occurrence for region 1, region 1.5, region 2, region 2.5, and region 3 are 24%, 39%, 27%, 7%, and 3%, respectively. The standard Supervisory Control and Data Acquisition (SCADA) system simultaneously records all turbine operational conditions at a sampling rate of 1 Hz.

B. Data preprocessing

We utilize a five-year Eolos dataset that consists of inflow wind conditions measured at the met tower and turbine operational conditions recorded in the turbine SCADA system to investigate the wind veer characteristics and their impact on turbine performance. The raw dataset (DS_i) with a sampling rate of 1 Hz is preprocessed following the procedures and criteria demonstrated in Fig. 2. The raw dataset is first smoothed by averaging consecutive sets of 120

data points (i.e., 2-min arithmetic averages based on 1 Hz raw data) to diminish high-frequency fluctuations associated with small-scale wind structures. To guarantee the met tower measurements represent the inflow conditions for the turbine, the lower and upper bounds (LB, UB) for the hub-height wind directions (θ_{hub}) are set to 90° and 270° , respectively. The corresponding wind direction change ($\Delta\theta$) falls in the range of -180° (lower bound of the wind direction change, $\Delta\theta_{LB}$) to 180° (upper bound of the wind direction change, $\Delta\theta_{UB}$). The remaining wind direction data are used for the calculation of the wind veer across the turbine rotor, i.e., $\gamma = (\theta_{TT} - \theta_{BT}) / (z_{TT} - z_{BT})$, where TT and BT are short for the blade top tip and bottom tip, respectively. Other outliers are detected using Grubbs’s test (assume following a normal distribution with a detection threshold factor ranging from 0 to 1, where values close to 0 result in a smaller number of outliers and values close to 1 result in a larger number of outliers) and discarded from the dataset with a threshold of 0.05. To have a better linkage between the inflow

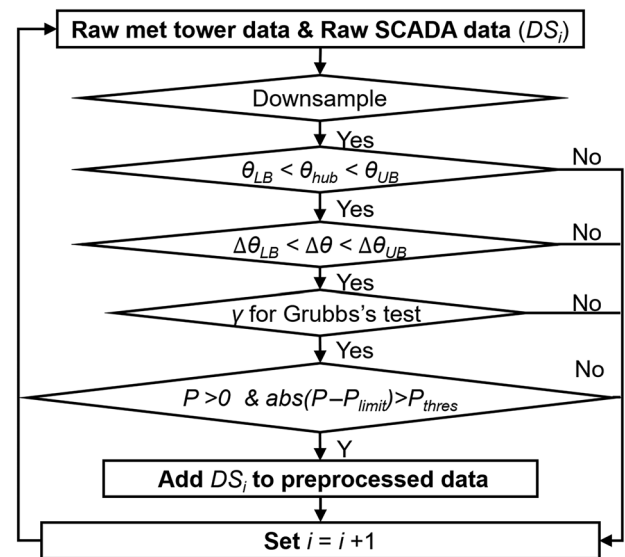


FIG. 2. Flowchart of the data preprocessing procedures and criteria for wind veer characterization.

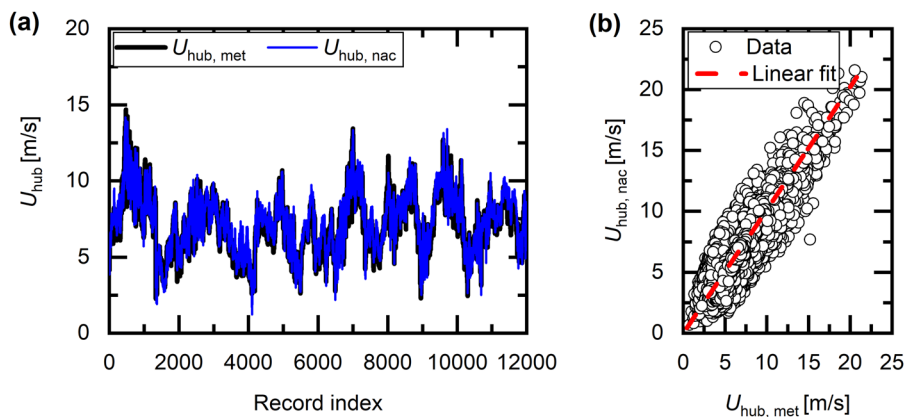


FIG. 3. Comparison between hub-height wind speeds measured at the met tower ($U_{hub,met}$) and the turbine nacelle ($U_{hub,nac}$), including (a) time series and (b) relevance analysis. The physical time stamp is not continuous due to data preprocessing, and the record index in (a) refers to the sequence number of the 2-min-averaged data point.

conditions and the turbine performance, the data with no power generation and affected by the curtailments are discarded by setting a threshold (P_{thres}) of 5% for the difference between the power (P) and the power limit (P_{limit}). After the applications of the quality control procedures and data clean criteria, there are 361 433 data points remaining (equivalent to 12 048 h) for the following analysis.

Figure 3 compares the hub-height wind speeds measured at the met tower ($U_{hub,met}$) and the turbine nacelle ($U_{hub,nac}$). The time variations of $U_{hub,met}$ and $U_{hub,nac}$ have a good agreement in general with a small mean difference of 0.2 m/s, as can be seen in Fig. 3(a). Additionally, the observations of $U_{hub,met}$ and $U_{hub,nac}$ are of high relevance with a linear slope close to 1.0 [Fig. 3(b)] and a high correlation (Pearson correlation coefficient: $\rho = 0.9340$, $p\text{-value} = 0.00$), indicating that the inflow conditions are well captured by the measurements at the met tower location.

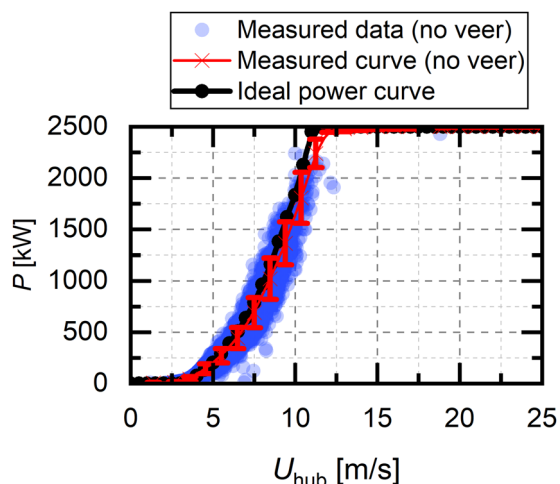


FIG. 4. Measured power curve of the Eolos turbine with a bin size of 1.0 m/s under no veer conditions ($\gamma < 0.01^\circ/\text{m}$). The error bars correspond to ± 1 standard deviation.

To determine the power deviation induced by the wind veer effect, the measured power curve under the no veer condition ($\gamma < 0.01^\circ/\text{m}$) is extracted from the simultaneously collected data of U_{hub} and power output (P) with a bin size of 1.0 m/s. Such no veer conditions take a proportion of 6% of the entire preprocessed dataset. As shown in Fig. 4, the measured power outputs oscillate around the ideal power curve (i.e., the manufacturer's reference values). The mean measured power curve is below the ideal power curve in most situations, with an overall loss of 12.2%. This measured curve is to be used as the baseline for the estimation of the power deviation (ΔP) due to wind veer in the following analysis.

III. RESULTS

A. Wind veer characterization and four scenarios

We first investigate the wind veer characteristics with the magnitudes of the wind veer across the entire turbine rotor (γ). The histogram in Fig. 5 shows the observed percent occurrence of γ , i.e., 42% for veering (clockwise rotating with height, positive values) and 58% for backing (counterclockwise rotating, negative values). Such a ratio is inverse to the offshore observations,²¹ mainly associated with the different thermal stratification behaviors in the offshore and onshore sites. The shape of such distribution features a narrow peak at a small negative angle with a broader right tail. It should be noted that although the peak yields at a negative angle, the mean wind veer of the entire dataset is positive ($0.002^\circ/\text{m}$) due to the higher probabilities of higher-magnitude veering winds (see the right tail of the distribution in Fig. 5), consistent with the Ekman spiral effect and inertial oscillation. Such a trend also matches the observations of wind veer measured between 10 m and 116 m levels at Lubbock, Texas.⁷

The variation of wind veer across the rotor may significantly affect the forces or loadings acting on the turbine blades. To provide more accurate assessments of the potential effect of wind veer, we propose to divide the wind veer conditions into four scenarios based on their changes in upper and lower rotors, as follows:

- Scenario VV: veering (upper rotor) and veering (lower rotor); see Fig. 6(a).

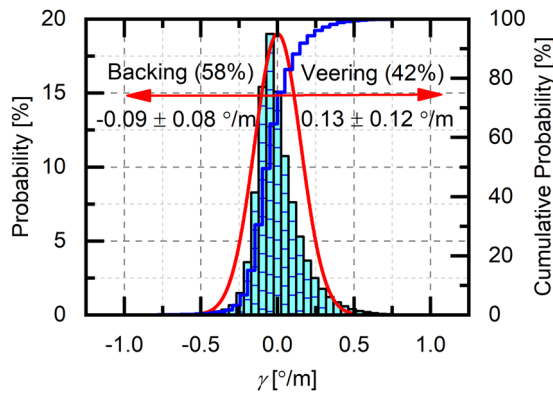


FIG. 5. Probability distribution of wind veer across the turbine rotor (γ). The red curve fits a normal distribution. The blue curve indicates the cumulative probability of wind veer.

- Scenario VB: veering (upper rotor) and backing (lower rotor); see Fig. 6(b).
- Scenario BV: backing (upper rotor) and veering (lower rotor); see Fig. 6(c).
- Scenario BB: backing (upper rotor) and backing (lower rotor); see Fig. 6(d).

Scenarios VV, VB, BV, and BB comprise 18%, 2%, 56%, and 24% of the entire dataset, respectively. Such predominant backing winds (BV, BB) are potentially associated with the location of the Eolos station that is in the vicinity of the low-pressure center and the relatively higher unstable atmospheric boundary layer. At this site, the stable, neutral, and unstable conditions comprise 24%, 21%, and 55% of a year, respectively, which dramatically differs from the observation at Lubbock, Texas⁷ (stable: 52% and unstable: 48%).

Figure 7 further compares the histograms of the wind veer across the turbine rotor (γ), upper rotor wind veer (γ_U), and lower rotor wind veer (γ_L) under the four scenarios. In most situations, the shape of the distributions of γ , γ_U , and γ_L yields peaks at small magnitudes and low-magnitude angles ($<0.3^\circ/\text{m}$) present over 80% of the time. γ is neutralized with the combined effect of γ_U and γ_L , particularly in VB and BV scenarios. More specifically, in VV and

VB scenarios, the distributions of γ_L exhibit broader tails compared with their distributions of γ_U with almost doubled mean absolute magnitudes. Such phenomena are primarily related to the strong wind shear at lower elevations.^{22,23} Reverse trends are observed in BV and BB scenarios that the distributions of γ_U exhibit higher probabilities at relatively high-magnitude angles than the distributions of γ_L with higher mean absolute magnitudes, potentially associated with the passage of cold fronts.²⁴ Additionally, in all four scenarios, the signals of γ_L yield stronger fluctuations than those of γ_U , mainly due to the higher turbulence levels at lower elevations.^{22,23}

To investigate the diurnal variation of wind veer, the observations are portioned based on the hour of the day. As shown in Fig. 8(a), the hourly averaged γ monotonously increases from the sunset at $\sim 18:00$ to the sunrise at $\sim 6:00$, associated with the evolving temperature field that does not reach equilibrium. The hourly averaged γ sharply decreases from $\sim 6:00$ to $\sim 10:00$ and then exhibits a “plateau” region from $\sim 11:00$ to $\sim 17:00$, associated with the consistent surface layer. A similar trend of the daily cycle of γ was observed on 1 August 2013 in a wind site in central Iowa.¹² Additionally, the daily variation of γ follows a similar trend to U_{hub} with a correlation of 0.75, as shown in Fig. 8(b). However, the fluctuations of these two variables are negatively correlated with a coefficient of -0.88 , suggesting that the limited changes in γ during the daytime may be related to the high turbulence levels at that time.²³ Note that the turbulence level is considered an independent variable in the above correlation analysis.

The hourly averaged γ_U and γ_L are well correlated [i.e., $\rho(\gamma_U, \gamma_L) = 0.99$] and follow similar trends to γ . The combined effect of γ_U and γ_L shows the hourly averaged γ tends to be backing in the daytime and veering in the nighttime. This trend matches well the atmospheric stability changes during a day that the Midwest region and Great Plains experience an energetically stable nocturnal and an unstable diurnal boundary layer.¹² The statically stable conditions permit a higher probability of higher-magnitude veering winds,⁷ which explains the prevailing veering conditions at nighttime in our field observations. Besides, the percent occurrences for the four scenarios are provided for each of the 24 h in a day in Fig. 8(c). The proportions of scenarios VV and BB exhibit significant opposite diurnal variations, while the changes in the other two scenarios are limited. Such ratios are

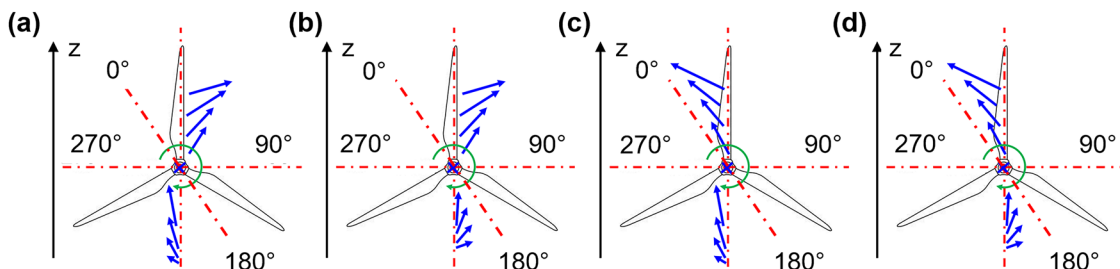


FIG. 6. Schematics illustrating the four scenarios of wind veer conditions: (a) VV, (b) VB, (c) BV, and (d) BB. The green arrow shows the rotational direction of the turbine rotor, i.e., clockwise (CW) for the Eolos turbine. Blue arrows represent wind velocity vectors. Suppose the inflow wind comes from the right south (180°) at hub height, i.e., pointing inside. The dashed-dotted lines point out the vertical, transverse (along W 270° and E 90°), and inflow directions (from S 180° to N 0°). The wind speed increases with height (z), i.e., wind shear. Veering and backing winds shift in clockwise and counterclockwise directions with height, respectively, in the Northern Hemisphere.

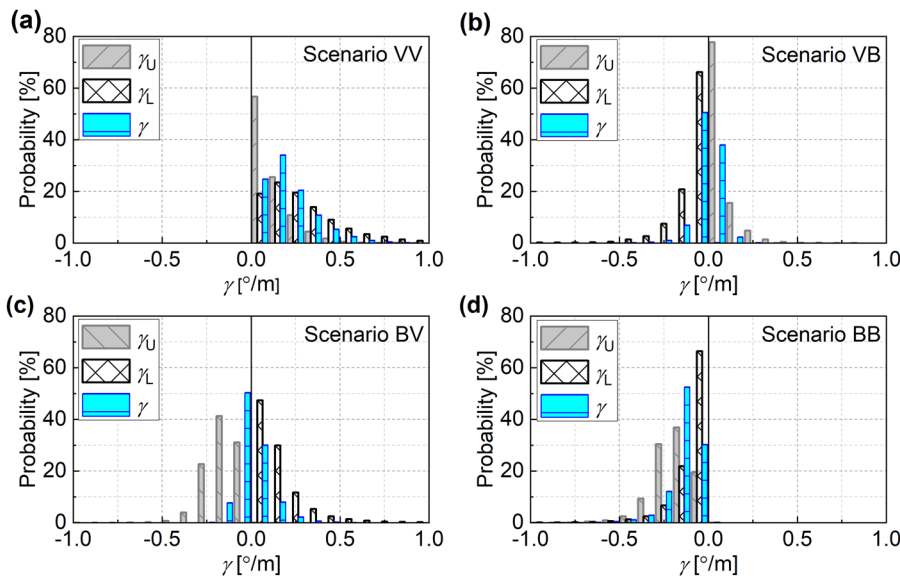


FIG. 7. Probability distribution for the wind veer across the turbine rotor (γ), upper rotor wind veer (γ_U), and lower rotor wind veer (γ_L) in four scenarios: (a) VV, (b) VB, (c) BV, and (d) BB. Bin size: $0.10^\circ/\text{m}$.

essential for the evaluation of turbine power performance in the Section II B.

Following the diurnal variation of wind veer, its annual variation is also studied by portioning the dataset based on the month of the year. Figure 9(a) shows the monthly averaged γ , γ_U , and γ_L and their fluctuations. The overall monthly averaged γ exhibits the negative values from April to August with decreasing U_{hub} and positive values from September to March, as shown in Fig. 9(b), similar to the unstable daytime and stable nighttime observations, respectively. Additionally, the upper rotor and lower rotor are also inclined to experience backing and veering winds in general. However, unlike the daily variations, the annual variations of these three angles are not that substantial, as indicated by the lower correlations [i.e., $\rho(\gamma_U, \gamma_L) = 0.60$, $\rho(\gamma, U_{hub}) = -0.37$, and $\rho(std(\gamma),$

$std(U_{hub})) = 0.40$]. Such reductions in the correlation coefficient may be associated with the influence of other atmospheric phenomena such as a low-level jet that usually occurs in Midwest areas. The percent occurrences of the four scenarios in each month, given in Fig. 9(c), provide a more direct view of the annual variation. Scenario VV takes slightly larger proportions in winter compared to other months. No consistent trends are found in other scenarios. The seasonal differences in this site [winter: $abs(\gamma) = 0.11^\circ/\text{m}$, summer: $abs(\gamma) = 0.10^\circ/\text{m}$] are much smaller than those [winter: $abs(\gamma) = 0.05^\circ/\text{m}$, summer: $abs(\gamma) = 0.10^\circ/\text{m}$] reported for a wind farm site off the Massachusetts coast, USA, by Bodini *et al.*,⁹ primarily related to the neutralization effects due to the complicated atmospheric boundary conditions of the Eolos site. Overall, in comparison with the weaker annual variation, the daily variation is more

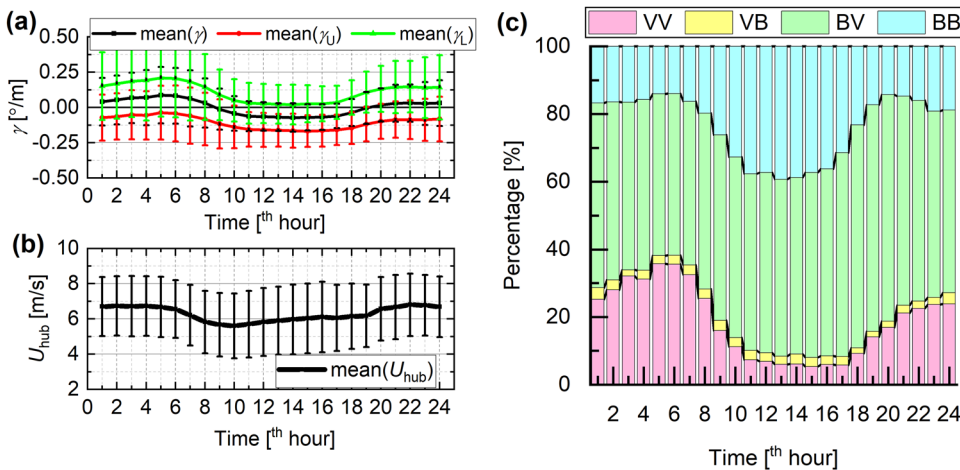


FIG. 8. Average diurnal variation of (a) wind veer characteristics, (b) hub-height wind speed, and (c) percent occurrence of each scenario. The error bars correspond to ± 1 standard deviation. Note that the time here refers to local time.

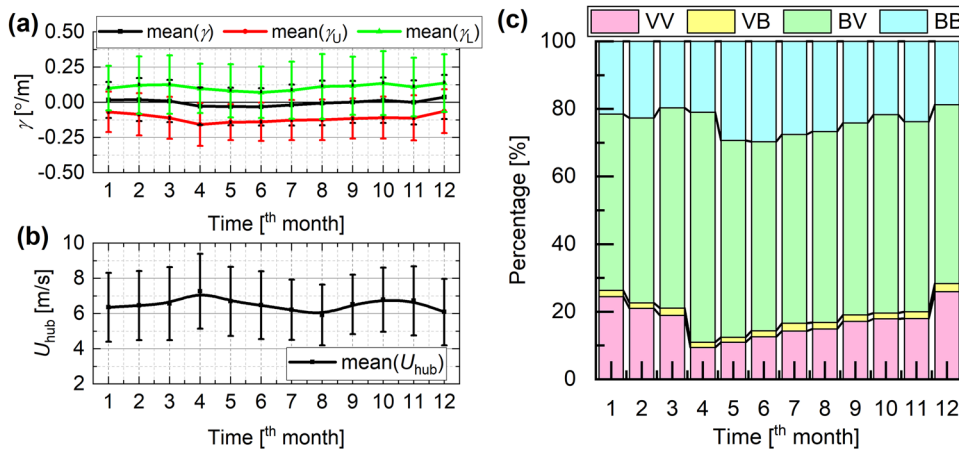


FIG. 9. Average annual variation of (a) wind veer characteristics, (b) hub-height wind speed, and (c) percent occurrence of each scenario. The error bars correspond to ± 1 standard deviation.

substantial and valuable for assessing the wind veer effect on turbine power production.

B. Wind veer induced power deviation

The effect of wind veer on turbine power production is then evaluated with the field dataset for the four scenarios, followed by a theoretical analysis of the underlying mechanism. The power deviation coefficient is defined as $PDC = (\sum \Delta P / \sum P_{mod}) \times 100\%$, where $\Delta P = P_{mea} - P_{mod}$, in which P_{mea} and P_{mod} refer to the measured power and modeled power, respectively. P_{mod} is modeled based on the sequence of $U_{hub,mac}$ and the measured power curve under no veer conditions depicted in Fig. 4 with a ninth-order polynomial fit. The negative and positive values of the PDC refer to power loss and power gain, respectively. As listed in Table I, the overall PDC for the entire dataset is very small, indicating that the overall effect of wind veer on the turbine power production is quite limited. However, the PDC s for VV, VB, BV, and BB scenarios are more substantial, suggesting that the underlying mechanism for the wind veer induced power deviation should be analyzed according to different scenarios.

Figure 10(a) compares the PDC s in different ranges of the magnitude of wind veer across the rotor, i.e., $abs(\gamma)$. In scenario VV, as the value of $abs(\gamma)$ increases, the PDC decreases correspondingly. In the range of $abs(\gamma) \in [0.6, 0.7](^\circ/m)$, the PDC declines to -18% , indicating that the larger wind veer tends to result in severer power loss. In scenario VB, the PDC decreases from -4% to

-26% , as the value of $abs(\gamma)$ increases from $0.01^\circ/m$ to $0.5^\circ/m$, and then increases back to -3% , as $abs(\gamma)$ continuously increases up to $0.7^\circ/m$. Such a pattern is also observed in scenario BV, which has a $\sim 2\%$ power gain in the lowest range of $[0.01, 0.1](^\circ/m)$. In scenario BB, the PDC yields positive values in the lowest two ranges below $0.2^\circ/m$ and decreases to -15% in higher ranges of $abs(\gamma)$. It should be noted that the turning points of trends are found at $abs(\gamma) \cong 0.5^\circ/m$ in all four scenarios. However, the data with $abs(\gamma) > 0.5^\circ/m$ are less than 5% of the entire dataset, as shown in Fig. 7.

Figure 10(b) shows the correlation coefficients of normalized upper-rotor wind veer and power deviations denoted $\rho(\gamma_U^*, \Delta P^*)$, as a function of $abs(\gamma)$. The variables are normalized using the maximum and minimum values in their corresponding datasets. It should be noted that we use γ_U , instead of γ , for the correlation analysis because γ_U is less influenced by the ground and tower shadow effects. All the four scenarios exhibit weak correlations between the two variables ($\gamma_U^*, \Delta P^*$) using the data satisfying $abs(\gamma) > 0.1^\circ/m$. Such correlations become much stronger as the sampling condition of $abs(\gamma)$ increases. When $abs(\gamma) > 0.4^\circ/m$, $\rho(\gamma_U^*, \Delta P^*)$ for VV, VB, BV, and BB are 0.29, 0.38, -0.59 , and -0.30 , respectively. This trend implies that the power deviation is more sensitive to high-magnitude veering or backing winds.

To have a better understanding of the findings derived from the field observations, we provide a theoretical analysis of the wind veer induced changes in the velocity triangle of a blade element. Figure 11 illustrates the change in the velocity triangle and corresponding turbine loading associated with wind veer using the clockwise-rotating (CW) turbine under the BV scenario as an example. In the analysis, we assume that the wind veer has a limited effect on the inflow speed (U_∞), turbine rotor speed (ω), and pitch angle (β). We suppose the inflow wind at hub height (U_{hub}) comes from the south (i.e., 180° , points inside). From the hub to the blade top tip (upper rotor), the inflow wind shifts counterclockwise as height increases, i.e., backing wind. From the blade bottom tip to the hub (lower rotor), the inflow wind moves clockwise with height, i.e., veering wind. In the velocity triangle, the relative velocity (U_{rel}) consists of the inflow component, i.e., $U_\infty(1 - a)$, and rotational component,

TABLE I. Power deviation under different scenarios based on the field dataset at the Eolos station.

Scenario	Percentage (%)	PDC (%)	Note
VV	18	-6.5	Loss
VB	2	-4.0	Loss
BV	56	0.2	Gain
BB	18	1.6	Gain
All	100	-0.008	Loss

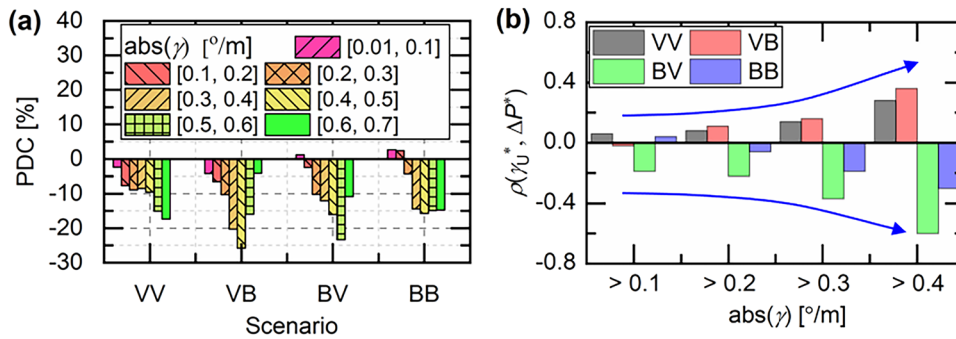


FIG. 10. (a) PDCs in different ranges of $abs(\gamma)$ and (b) correlation coefficient between the normalized upper-rotor wind veer and the power deviation denoted $\rho(\gamma_U^*, \Delta P^*)$ as a function of $abs(\gamma)$ in four scenarios. Note that even the smallest data sample contains sufficient data (240 points) to derive the correlation coefficient.

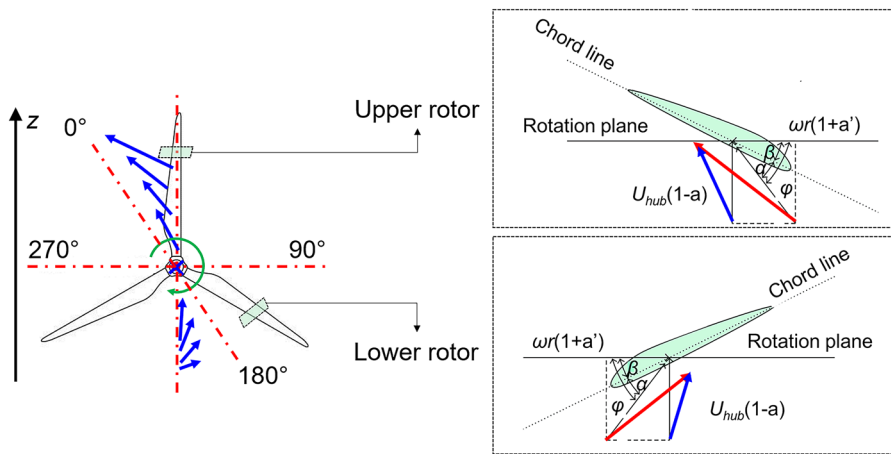


FIG. 11. Schematics illustrating the underlying mechanism of the wind veer effect on turbine power production with an example of a CW turbine in scenario BV.

i.e., $\omega r(1 + a')$, where a and a' are the axial and angular induction factors, respectively. In the upper rotor, the backing wind leads to a decrease in the inflow angle (φ). As φ decreases, the angle of attack (α) decreases, while U_{rel} increases, as highlighted in red in Fig. 11. In the lower rotor, the veering wind results in an increment in φ , and thus, the corresponding α increases and U_{rel} decreases. Wind turbines are designed to operate with the optimal α associated with the maximum lift-to-drag ratio (C_L/C_D) for the most aerodynamically efficient operation, i.e., optimal power coefficient $C_{P,opt}$. The

changes in α , regardless of increase and decrease, yield a reduction in C_P and, in turn, power output ($P \propto C_P$). Additionally, a larger U_{rel} corresponds to a larger lift force acting on the blade element ($F_L \propto U_{rel}^2$), which increases the turbine power output, and vice versa. Note that the above analysis is suitable for the wind turbine operating under variable-speed regulations (i.e., region 1.5, region 2, and region 2.5 in our case). It should be cautioned to extend the analysis to the turbine in operation of variable-pitch regulations (i.e., region 3).

TABLE II. Theoretical analysis of the power deviation in four scenarios for CW and CCW turbines (note that the symbols +, -, ~ refer to the trends of increase, decrease, and remaining the same).

Scenario	CW turbine				CCW turbine		
	$\Delta\alpha_U / \Delta\alpha_L$	$\Delta U_{rel,U} / \Delta U_{rel,L}$	ΔP	PDC (field data) (%)	$\Delta\alpha_U / \Delta\alpha_L$	$\Delta U_{rel,U} / \Delta U_{rel,L}$	ΔP
VV	+/+	-/-	-	-6.5	-/-	+/+	+/~/-
VB	+/-	-/+	-/~/+	-4.0	-/+	+/-	~/+/-
BV	-/+	+/-	~/+/-	0.2	+/-	-/+	-/~/+
BB	-/-	+/+	+/~/-	1.6	+/+	-/-	-

We conduct the same analysis for all four scenarios, and the changes in α and U_{rel} are listed in Table II. In scenario VV, the variations in α and U_{rel} suggest a power decrease. The larger $abs(\gamma)$ can enlarge the changes in α and U_{rel} , contributing to more substantial power losses, consistent with our field observation. In scenarios VB and BV, their upper and lower rotor changes in ΔU_{rel} , i.e., $\Delta U_{rel,U}$ and $\Delta U_{rel,L}$, have trade-off effects on the turbine power deviations. The wind veer effect on the upper rotor is more significant than that on the lower rotor, primarily because the higher wind speeds at higher elevations are less influenced by the ground interaction and tower shadow. As a result, scenarios VB and BV tend to have small power losses and power gains, respectively. Besides, α varies significantly under a larger $abs(\gamma)$ condition, which may lead to a detrimental effect on the power output and support the corresponding field findings of low PDC s in Fig. 10(a). In scenario BB, the increase in U_{rel} is inclined to generate appreciable power gains, while the changes in α may eliminate such benefits, in good agreement with our field observations. Note that unlike the wind shear flows with a stronger effect on the upper rotor, the uniform inflows tend to have equal effects on the upper and lower rotors.

It should be noted the turbine rotor rotating direction plays an essential role in estimating the wind veer effect on turbine power production in each scenario. Table II compares the analysis results for a turbine with different rotation directions, i.e., clockwise (CW) and counterclockwise (CCW). Interestingly, the estimated power deviations in scenarios VV, VB, BV, and BB for a CW turbine correspond to the results in scenarios BB, BV, VB, and VV for the CCW turbine.

Based on the daily variation of percent occurrences of the four scenarios shown in Fig. 8(c) and the corresponding PDC values listed in Table II, the power deviation for each hour of the day is estimated using Eq. (1). The estimation has a strong correlation with the field observation of 0.88. As shown in Fig. 12, the turbine is more likely to yield power loss and gain during nighttime and daytime, respectively,

$$PDC = w_{VV}PDC_{VV} + w_{VB}PDC_{VB} + w_{BV}PDC_{BV} + w_{BB}PDC_{BB}, \quad (1)$$

where w presents the weight of the scenario, corresponding to its occurrence percentage.

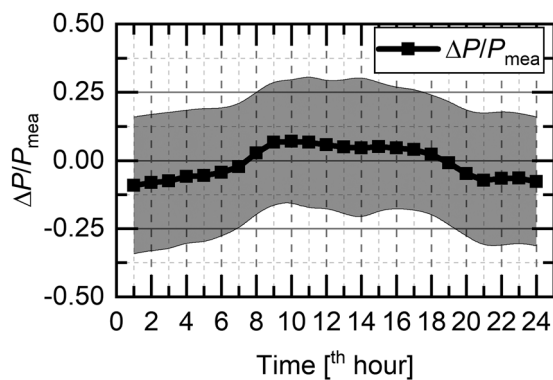


FIG. 12. Average diurnal variation of the normalized power deviation ($\Delta P/P_{mea}$). The gray shaded region corresponds to ± 1 standard deviation.

IV. CONCLUSION AND DISCUSSION

The present study investigates the wind veer characteristics and their impact on the power performance of a utility-scale wind turbine (2.5 MW) using a five-year field dataset measured at the Eolos Wind Energy Research Station of the University of Minnesota in Rosemount, Minnesota ($44^{\circ}44'01.4''N$, $93^{\circ}05'04.4''W$). This field dataset consists of the turbine operational conditions recorded in the turbine SCADA system and inflow conditions for wind veer characterization measured with a well-instrumented met tower located $1.77 D$ upstream of the turbine. At the Eolos station, although there are more backing wind cases than the veering cases, the overall wind veer across the rotor exhibits a small positive value of $0.002^{\circ}/m$ (i.e., veering), associated with higher probabilities of higher-magnitude veering winds. Such a trend is consistent with the Ekman spiral effect and inertial oscillation in the Northern Hemisphere and also matches the observations at Lubbock, Texas.⁷ The main contributions/findings are summarized below.

We propose to divide the wind veer conditions into four scenarios based on their changes in turbine upper and lower rotors: VV (upper rotor: veering, lower rotor: veering), VB (upper rotor: veering, lower rotor: backing), BV (upper rotor: backing, lower rotor: veering), and BB (upper rotor: backing, lower rotor: backing). The presence and proportion of different scenarios are strongly associated with the geographic location of a turbine site. In our case, scenarios VV, VB, BV, and BB comprise 18%, 2%, 56%, and 24% of the entire dataset, respectively, which are potentially associated with the location of the Eolos station in the vicinity of the low-pressure center and the relatively higher unstable atmospheric boundary layer. Besides, the occurrence ratio of different scenarios exhibits a clear diurnal pattern. Scenario VV is more likely to occur during the stable nighttime periods, while scenario BB tends to occur during the daytime with convective/unstable flows. The other two scenarios almost have the same proportions throughout a day. Such trends agree with the field observations in Lubbock, Texas,⁷ and central Iowa,¹² suggesting to be generalizable in most onshore wind sites in the Northern Hemisphere. In comparison with the diurnal variation, the annual variation is relatively inappreciable in our site, unlike the significant seasonal differences reported for an offshore site off the Massachusetts coast.⁹ Moreover, our observation shows that in scenarios VV and VB, the upper-rotor wind veer (γ_U) exhibits higher magnitudes (doubled) than those of the lower rotor (γ_L), primarily related to the strong wind shear at lower elevations.^{22,23} Reverse trends observed in scenarios BV and BB are potentially associated with the passage of cold fronts.²⁴

The division of wind veer into different scenarios allows us to elucidate its impact on turbine power generation. For clockwise (CW) turbines (like the Eolos turbine in our case), substantial power loss is expected in scenario VV ($\sim 6.5\%$ in our case), while a small amount of power gain can occur in scenario BB ($\sim 1.6\%$ in our case). In comparison with scenarios VV and BB, the power deviations in scenarios VB and BV are relatively smaller due to the neutralization of the upper and rotor behaviors. Such field assessment is supported by a theoretical analysis of the velocity triangle of a blade element. The main influences of wind veer are the variations in the angle of attack (α) and relative wind speed (U_{rel}). The veering wind tends to

lead to the increase in α and the decrease in U_{rel} . In contrast, the backing wind tends to result in the decrease in α and the increase in U_{rel} , consistent with the simulations by Wagner *et al.*²⁵ These changes may significantly degrade the designed power coefficient and modify the aerodynamic forces acting on the blades, resulting in substantial power deviations. Additionally, the turbine rotational direction plays a vital role in the turbine power generation under wind veer conditions. The counterclockwise (CCW) turbine follows an exactly opposite trend to the CW turbine, i.e., the estimated power deviations in scenarios VV, VB, BV, and BB for a CCW turbine are equivalent to the results in scenarios BB, BV, VB, and VV for a CW turbine.

The aforementioned findings can provide practical guidance for the wind farm macro/micro-siting to achieve the maximum profits. Based on the proportion of different scenarios that depends on the geographic location of the turbine site, our study provides a direct formulation to estimate the power losses associated with the wind veer, which can be used as a valuable reference for the decision making of wind site investment, particularly in the trend of turbine maximization. Furthermore, we suggest introducing wind veer as a valid index in the standard wind resource assessment. Specifically, based on the proportion of different scenarios estimated based on the one-year met tower data before the wind farm construction, wind farm operators can select proper types of wind turbines in terms of turbine rotational direction for more power generation. CCW turbines are more advantageous if the site prevails with scenarios VV and VB. Otherwise, CW turbines are suggested. Moreover, the adjustment of the turbine rotational direction according to the diurnal variation of wind veer can also be beneficial for the turbine power generation. Operations in the counterclockwise rotation mode and clockwise rotation mode are profitable at nighttime and daytime, respectively, for onshore wind sites in the Northern Hemisphere. Such improvements require a novel design of the symmetric blades.

Nevertheless, it should be noted that the field measurements of the wind directions used for the wind veer calculation involve a small uncertainty on the order of $0.01^\circ/\text{m}$ (i.e., $\pm 0.7^\circ$ across the entire span of the rotor), which is negligible and treated as the no veer condition in the present study. In addition, the Eolos turbine has a small chance (4%) to operate in region 3 with variable-pitch regulation. The field measurements mainly support the findings when the turbine is in the variable-speed regulation regions (region 1.5, region 2, and region 2.5). It should be cautioned to extend the derived field measurement results and theoretical analysis to region 3 of the turbine with pitch regulations.

ACKNOWLEDGMENTS

This work was supported by the National Science Foundation CAREER award (Grant No. NSF-CBET-1454259), Xcel Energy through the Renewable Development Fund (Grant No. RD4-13), and IonE of the University of Minnesota. The authors thank the engineers from St. Anthony Falls Laboratory, including Christopher Milliren, Chris Feist, and Matthew Lueker, for the fruitful discussion regarding the Eolos database.

DATA AVAILABILITY

The data that support the findings of this study are available within this article and from the corresponding author upon reasonable request.

REFERENCES

- J. R. Holton and G. J. Hakim, "Chapter 8 - The planetary boundary layer," in *An Introduction to Dynamic Meteorology*, (Elsevier, 2013), pp. 255-277..
- H. Lu and F. Porté-Agel, "Large-eddy simulation of a very large wind farm in a stable atmospheric boundary layer," *Phys. Fluids* **23**, 065101 (2011).
- C. VerHulst and C. Meneveau, "Large eddy simulation study of the kinetic energy entrainment by energetic turbulent flow structures in large wind farms," *Phys. Fluids* **26**, 025113 (2014).
- D. Allaert and J. Meyers, "Large eddy simulation of a large wind-turbine array in a conventionally neutral atmospheric boundary layer," *Phys. Fluids* **27**, 065108 (2015).
- W. Tian, A. Ozbay, and H. Hu, "Effects of incoming surface wind conditions on the wake characteristics and dynamic wind loads acting on a wind turbine model," *Phys. Fluids* **26**, 125108 (2014).
- M. Bastankhah and F. Porté-Agel, "Wind tunnel study of the wind turbine interaction with a boundary-layer flow: Upwind region, turbine performance, and wake region," *Phys. Fluids* **29**, 065105 (2017).
- K. Walter, C. C. Weiss, A. H. P. Swift, J. Chapman, and N. D. Kelley, "Speed and direction shear in the stable nocturnal boundary layer," *J. Sol. Energy Eng.* **131**, 0110131 (2009).
- M. Abkar, A. Sharifi, and F. Porté-Agel, "Wake flow in a wind farm during a diurnal cycle," *J. Turbul.* **17**, 420 (2016).
- N. Bodini, J. K. Lundquist, and A. Kirincich, "U.S. East coast lidar measurements show offshore wind turbines will encounter very low atmospheric turbulence," *Geophys. Res. Lett.* **46**, 5582, <https://doi.org/10.1029/2019gl082636> (2019).
- L. M. Bardal, L. R. Sætran, and E. Wangsnæs, *Performance Test of a 3MW Wind Turbine - Effects of Shear and Turbulence* (Elsevier, 2015).
- Y. Sakagami, P. A. Santos, J.C. P. Reinaldo and F.F. Taves, in EWEA Annual Event, 2015.
- M. Sanchez Gomez and J. K. Lundquist, "The effect of wind direction shear on turbine performance in a wind farm in central Iowa," *Wind Energy Sci.* **5**, 125 (2020).
- M. P. van der Laan and N. N. Sørensen, "Why the Coriolis force turns a wind farm wake clockwise in the Northern Hemisphere," *Wind Energy Sci.* **2**, 285 (2017).
- M. F. Howland, A. S. Ghate, and S. K. Lele, "Influence of the horizontal component of Earth's rotation on wind turbine wakes," *J. Phys.: Conf. Ser.* **1037**, 072003 (2018).
- A. Englberger, A. Dörnbrack, and J. Lundquist, "Does the rotational direction of a wind turbine impact the wake in a stably stratified atmospheric boundary layer?," *Wind Energy Sci. Discuss.* **20**, 1 (2019).
- S. N. Gadde and R. J. A. M. Stevens, "Effect of Coriolis force on a wind farm wake," *J. Phys.: Conf. Ser.* **1256**, 012026 (2019).
- M. Toloui, S. Riley, J. Hong, K. Howard, L. P. Chamorro, M. Guala, and J. Tucker, "Measurement of atmospheric boundary layer based on super-large-scale particle image velocimetry using natural snowfall," *Exp. Fluids* **55**, 1-14 (2014).
- T. Dasari, Y. Wu, Y. Liu, and J. Hong, "Near-wake behaviour of a utility-scale wind turbine," *J. Fluid Mech.* **859**, 204 (2019).
- L. P. Chamorro, S.-J. Lee, D. Olsen, C. Milliren, J. Marr, R. E. A. Arndt, and F. Sotiropoulos, "Turbulence effects on a full-scale 2.5 MW horizontal-axis wind turbine under neutrally stratified conditions," *Wind Energy* **18**, 339 (2015).
- L. P. Chamorro, J. Hong, and C. Gangodagamage, "On the scale-to-scale coupling between a full-scale wind turbine and turbulence," *J. Turbul.* **16**, 617 (2015).
- N. Bodini, J. K. Lundquist, R. Krishnamurthy, M. Pekour, L. K. Berg, and A. Choukulkar, "Spatial and temporal variability of turbulence

dissipation rate in complex terrain,” *Atmos. Chem. Phys.* **19**, 4367 (2019).

²²L. Gao, S. Yang, A. Abraham, and J. Hong, “Effects of inflow turbulence on structural response of wind turbine blades,” *J. Wind Eng. Ind. Aerodyn.* **199**, 104137 (2020).

²³L. Tian, Y. Song, N. Zhao, W. Shen, T. Wang, and C. Zhu, “Numerical investigations into the idealized diurnal cycle of atmospheric boundary layer and

its impact on wind turbine’s power performance,” *Renewable Energy* **145**, 419 (2020).

²⁴S. Emeis, *Wind Energy Meteorology* (Springer International Publishing, Cham, 2018).

²⁵R. Wagner, M. S. Courtney, T. J. Larsen, and U. S. Paulsen, “Simulation of shear and turbulence impact on wind turbine performance,” Riso-R-Report No. 1722(EN), 2010.